46th AIAA Aerospace Sciences Meeting and Exhibit
7 - 10 January 2008, Reno, Nevada

AIAA 2008-1249

Nitric Oxide Production from Surface Recombination of Oxygen and Nitrogen Atoms

Dušan A. Pejaković* and Jochen Marschall†
SRI International, Menlo Park, CA, 94025

and

Lian Duan‡ and Maria P. Martin§
Princeton University, Princeton, New Jersey 08544

Experimental results are presented that support the surface-catalyzed production of nitric oxide from the recombination of oxygen and nitrogen atoms on quartz. The experiments employ two-photon laser induced fluorescence detection of atomic oxygen and atomic nitrogen to characterize changes in gas-phase atom concentrations as the ratio of O to N atoms is varied at the opening of a diffusion-tube side-arm reactor. The measurements verify a correlation between decreased O-atom loss and enhanced N-atom loss in N_2/N/O mixtures. Computational simulations of the side-arm reactor with a multi-species reaction-diffusion model strengthen the case for NO surface formation, reproducing observed changes in O- and N-atom concentration profiles with varying O/N ratios at the side-arm entrance when surface-catalyzed NO production is included in the boundary conditions.

Nomenclature

c	=	concentration or molar density, mol m^{-3}
D	=	diffusion coefficient, m^2 s^{-1}
F	=	volumetric flow rate, sccm
$f_{s,r}$	=	branching fraction of reactant s into product r
j	=	diffusive mass flux, kg m^{-2} s^{-1}
k_B	=	Boltzmann's constant 1.381×10^{-23} J K^{-1}
L	=	side-arm reactor length, m
M	=	molar mass, kg mol^{-1}
N_{avo}	=	Avogadro's number, 6.022×10^{23} mol^{-1}
P	=	pressure, Pa
R	=	side-arm radius, m
r	=	radial side-arm coordinate, m
$\Re$	=	universal gas constant, 8.314 J mol^{-1} K^{-1}
T	=	temperature, K
v	=	bulk flow speed, m s^{-1}
$\bar{v}$	=	average thermal speed, m s^{-1}
υ	=	diffusion velocity, m s^{-1}
w	=	gas-phase production rate, kg m^{-3} s^{-1}
w_w	=	surface production rate, kg m^{-2} s^{-1}

* Research Physicist, Molecular Physics Laboratory; dusan.pejakovic@sri.com.
† Senior Research Scientist, Molecular Physics Laboratory; jochen.marschall@sri.com. Senior Member AIAA.
‡ Graduate Student, Mechanical and Aerospace Engineering Department; lduan@Princeton.EDU.
§ Assistant Professor, Mechanical and Aerospace Engineering Department; pmartin@Princeton.EDU. Senior Member AIAA.

x = mole fraction
z = axial side-arm coordinate, m
$\pi\overline{\Omega}_{rs}^{(1,1)}$ = collision integral, m^2
ω_s = weighting factor, Eq. 4
ρ = mass density, kg m^{-3}
γ = loss probability
μ = viscosity, Pa-s

Subscripts
O, O_2, N, N_2, NO = species
s = species index
r = species index or radial direction
w = wall
z = axial direction

I. Introduction

HETEROGENEOUS recombination of dissociated species on the surface of thermal protection system (TPS) materials is known to contribute to the aerothermal heating of hypersonic reentry vehicles. In the Earth's atmosphere, oxygen and nitrogen atoms are generated in the shock layer ahead of leading edges during hypersonic flight. Modeling O- and N-atom surface-catalyzed recombination is an important part of computational fluid dynamics (CFD) simulations that predict aerothermal heating as a function of flight trajectory.

Traditionally, CFD aerothermal heating computations have treated oxygen and nitrogen recombination as two uncoupled parallel processes, $O + O \rightarrow O_2$ and $N + N \rightarrow N_2$, neglecting the possibility of NO formation via O + N surface reactions. This choice is partly a matter of computational convenience and partly due to the lack of experimental information on the importance of the NO formation pathway. More recent modeling efforts have introduced finite-rate kinetic models to better capture the physics of surface catalytic reactions.[1-7] In at least one case, the inclusion of NO surface formation in a finite-rate surface chemistry model seems to improve agreement between aerothermal heating computations and measured flight data.[5] Strong support for NO surface formation is also provided by the *in situ* laser-induced fluorescence (LIF) detection of different NO concentrations in front of different materials tested in a plasma wind tunnel.[8]

Copeland *et al.*[9] reported an experimental approach for inferring the formation of NO in N_2/N/O gas mixtures using two-photon LIF detection of N atoms in a room-temperature diffusion-tube side-arm reactor. In the side-arm reactor technique, atomic species are generated in a main flow tube and diffuse into the opening of a dead-end side-arm tube where they are lost by gas-phase and surface-mediated recombination reactions, establishing a steady-state decaying atom concentration profile along the length of the side-arm tube. At sufficiently low pressures, heterogeneous atom loss processes dominate over (most) gas-phase reactions, and this atom concentration profile can be related to the catalytic activity of the tube surface.[10-17]

Copeland *et al.*[9] produced a range of N_2/N/O gas mixtures in the main flow tube by titrating a partially dissociated nitrogen flow with controlled amounts of NO to drive the gas-phase reaction $N + NO \rightarrow N_2 + O$. This bimolecular reaction produces one oxygen atom for every NO consumed and is very rapid with a room temperature rate coefficient[18] of 3×10^{-11} cm^3 $molecule^{-1}$ s^{-1}. They then demonstrated that, as O atoms were added to the flowing N_2/N mixture, the loss of N atoms from the gas phase within the side-arm tube increased. They interpreted this accelerated N-atom loss as resulting from the same gas phase $N + NO \rightarrow N_2 + O$ reaction, where the NO source was now N + O surface recombination on the walls of the side-arm tube.

Under the low pressures of their experiment (13 to 65 Pa), the direct production of NO in the gas phase by the three-body N + O + M reaction was insignificant.[19] Because the $N + NO \rightarrow N_2 + O$ reaction is so fast and atom concentrations in the side-arm reactor are low, the steady-state gas-phase NO concentrations generated by surface recombination are too small for direct LIF detection, and NO surface formation must be inferred indirectly from observed changes in atom concentrations.

Copeland *et al.*[9] suggested a further check of their interpretation: if surface NO formation was indeed occurring, O-atom loss from the gas phase should decrease with the addition of N atoms, since each reaction event N + NO regenerates a gas-phase O atom. However, they did not perform O-atom LIF measurements to confirm this.

We have repeated and extended the measurements of Copeland *et al.*[9] by adding, i) a more powerful discharge source for N-atom production, ii) the capability for sequential N-atom and O-atom LIF diagnostics, and iii) simultaneous concentration measurements at four different side-arm locations. The new experiments confirm the predicted correlation of decreased O-atom loss with enhanced N-atom loss, thus strengthening the case for surface production of NO. We investigate the relative importance of the NO surface production pathway to the O + O and N + N surface recombination reactions, by simulating the experimental results using a multi-species reaction-diffusion model.

II. Experiment

The layout of our experiment is shown in Fig.1. A partially-dissociated nitrogen flow is produced by metering nitrogen (99.999% purity) through a 6 kW microwave discharge using a 500 standard cubic centimeter per minute (sccm) Tylan mass flow controller. The main tube is made of glass and the side-arm tube is made of GE214 quartz. With valve 1 open and valve 2 closed, the partially-dissociated gas flows down the main arm, past the opening of the dead-end side-arm tube, and into a roots blower vacuum system. In this configuration the side-arm operates as a diffusion tube. The side-arm can be reconfigured as a flow tube by closing valve 1 and opening valve 2. Gas pressures are measured near the opening (port A) and near the end (port B) of the side-arm tube using a 10 Torr capacitance manometer with four digit precision and an error of less than 1%.

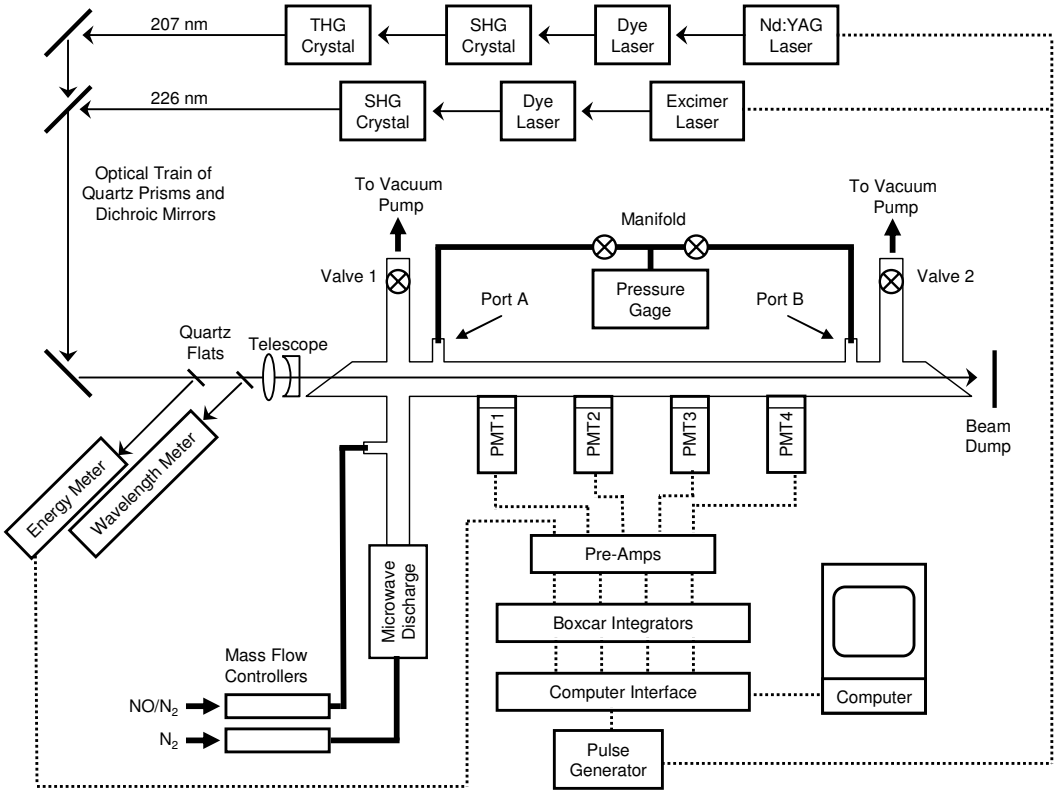

Figure 1. Experimental setup; PMT, SHG, and THG indicate photomultiplier tube, second harmonic generation and third harmonic generation, respectively.

Species detection was accomplished using well-known 2-photon LIF schemes: excitation at 226 nm followed by fluorescence at 845 nm for O-atoms[20,21] and excitation at 207 nm followed by fluorescence at 745 nm for N-atoms.[22] For O-atom LIF, a Lambda-Physik ENG 103 XeCl Excimer laser was used to pump a Lambda-Physik FL 3002 dye laser filled with Coumarin 47 laser dye dissolved in methanol. The resulting tunable output near 452 nm was frequency-doubled using a type B beta barium-borate (BBO) crystal to produce 226 nm radiation. For N-atom LIF,

tunable output near 621 nm was produced by pumping a Quanta-Ray MC1 dye laser filled with Rhodamine 640 dissolved in methanol, with the second harmonic output of a Quanta-Ray DCR-3 Nd:YAG laser. The red light was frequency tripled to produce 207 nm radiation using type 2 and type C BBO crystals for frequency doubling and frequency mixing, respectively.

The two ultraviolet laser beams were alternately directed through a quartz Brewster angle window down the centerline of the side-arm tube using different combinations of dichroic mirrors, quartz prisms and collimating optics. A Pellin-Broca prism was used to separate visible from ultraviolet light during the O-atom detection experiments; dichroic mirrors were sufficient to separate visible from UV light during the N-atom experiments. Quartz flats were used to direct small fractions of the laser beams into a Molectron pyroelectric energy meter and into a Coherent wavemeter, to monitor laser pulse energy and wavelength, respectively. The ultraviolet excitation energy per laser pulse was ~0.5 mJ for O-atom detection and ~0.1 mJ for N-atom detection.

Fluorescence was collected at right angles to the side-arm tube by four red-sensitive Hamamatsu photomultiplier tubes (R636) in gated sockets, fitted with 3 nm bandwidth interference filters centered on 845 nm for O-atom detection and 745 nm for N-atom detection. PMT signals were amplified by a factor of five and averaged over 150 ns wide gates using Stanford Research Systems (SRS) boxcar integrators. Data acquisition and laser firing were synchronized at 10 Hz using a SRS digital delay generator. Automation of the experiment and data collection was performed by a personal computer using LabView software.

The concentration of O atoms in the main gas flow was controlled by adding a 1%NO in N_2 gas mixture (99.5% pure NO in 99.999% pure N_2) to the partially-dissociated nitrogen flow upstream of the side-arm opening. At the N + NO titration endpoint all N atoms are consumed and replaced in the flow by O atoms. The titration endpoint can be detected by the disappearance of the N-atom LIF signal and the leveling off of the O-atom LIF signal.

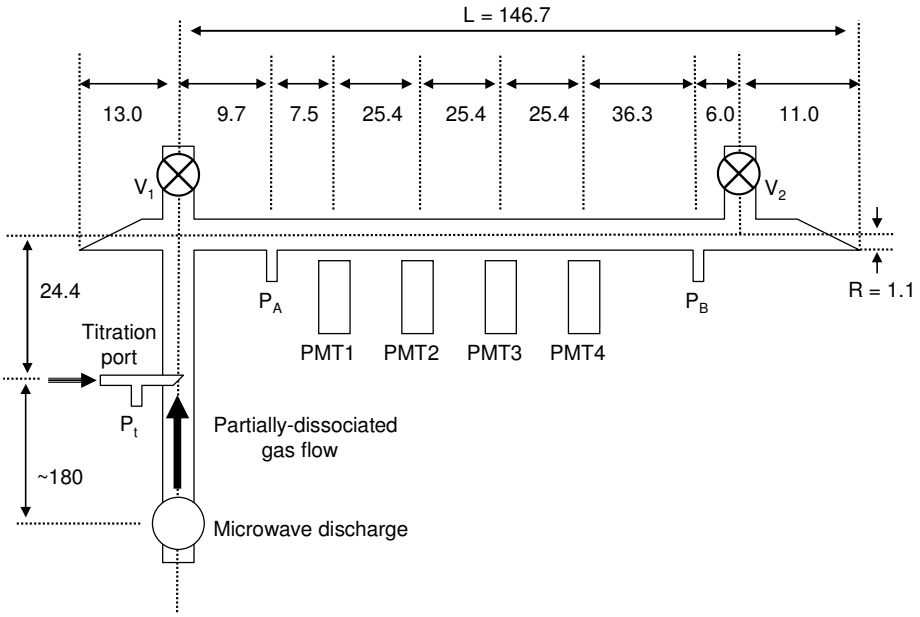

Figure 2. Important side-arm dimensions (in cm); drawing not to scale.

The experiments we report were conducted at 298 K, with a 44.4 sccm flow of N_2 into the main arm and the discharge operating at 40% of its maximum capacity (corresponding to ~2.4 kW.) The pressure at port A before any addition of the NO/N_2 gas mixture at the titration port was adjusted to be 60 Pa in both flow tube and diffusion tube experiments, by throttling the flow with the appropriate valve. The maximum gas flow added at the titration port was ~6 sccm, which increased the pressure at port A by about 1.3 Pa in both flow and diffusion tube modes. In flow tube mode, the pressure difference between ports A and B was approximately 5.3 Pa for all levels of added titration gas flows, resulting in bulk flow velocities ranging from about 3.6 to 3.85 m s^{-1} at the different PMT locations. Important experimental dimensions are shown in Fig. 2. The spacing between PMTs was 25.4 cm and the spacing between pressure ports A and B was 120 cm. The inner diameter of the side-arm tube was 2.2 cm.

III. Experimental Results

A. Qualitative Behavior

Figure 3a-d shows the variation in relative atom concentration as a function of the flow rate of NO added at the titration port for both N atoms and O atoms with the side-arm reactor configured as either a flow tube or a diffusion tube. The raw LIF data collected by each PMT were corrected for scattered light contributions by subtracting the off-resonance signals (corrections were always 3% or less of the total signal), normalized by the square of the laser pulse energy, and averaged over at least 200 laser shots at each added NO flow setting. The averaged data reflect changes in atom concentration at the particular PMT location with NO additions at the titration port. To better illustrate common behaviors in Figs. 3a-d the averaged values were then brought to a common scale by dividing each PMT data set by its maximum value.

With the side-arm tube configured as a flow tube, both the N-atom and the O-atom concentrations vary approximately linearly as NO is added at the titration port (except in the region near zero in the N-atom case; this is discussed in the following subsection.) When the reactor is switched to diffusion tube mode, clear deviations from this linear dependence are evident.

In Fig. 3b, the N-atom concentration decreases faster with added NO, producing a concave profile, while in Fig. 3d the O-atom profile becomes convex, consistent with a faster rise in O-atom concentration with added NO. The result shown in Fig. 3b reproduces the experimental observations of Copeland *et al.*[9] for N atoms, and the result shown in Fig. 3d confirms their predictions for O atoms. Copeland *et al.*[9] also found a trend of increasing deviation from linearity with increasing distance from the side-arm opening. Despite experimental scatter, similar trends are found in the present measurements, and especially when comparing PMT1 (solid circles) and PMT4 (open triangles) data near the midpoint of the titration curve. Thus, the current measurements support and strengthen the hypothesis of NO formation by surface reactions.

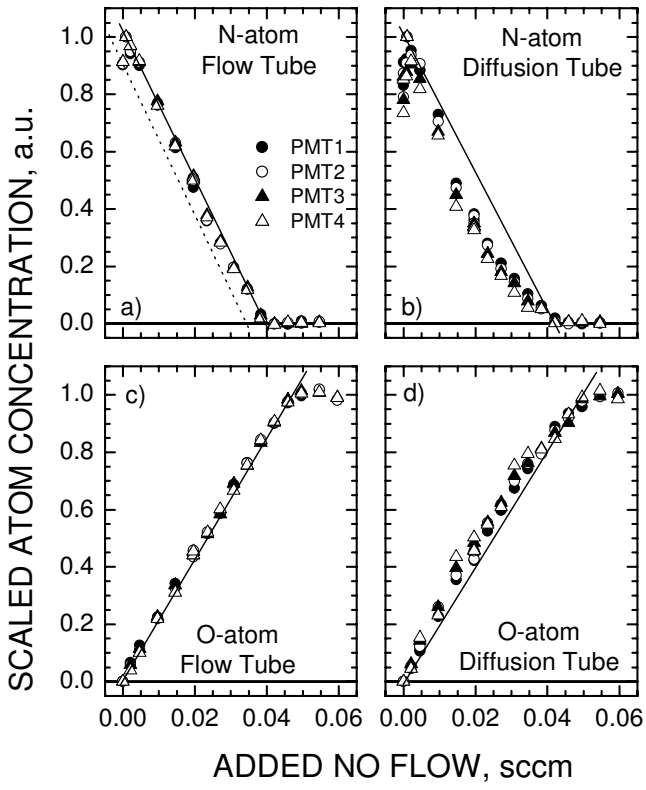

Figure 3. Variations in the scaled atom concentrations measured at the four PMT locations with the addition of NO at the titration port: a) N atoms in flow tube, b) N atoms in diffusion tube, c) O atoms in flow tube, and d) O atoms in diffusion tube. Solid lines are guides for the eye; the offset dashed line in Fig. 3a is discussed in the text.

In order to compare experimental data with the predictions of a multi-species reaction-diffusion model, the scaled measurements of Figs. 3b and 3d must be corrected for variations in LIF detection sensitivities at the different PMT locations and the absolute atom concentrations at the side-arm opening must be determined.

B. Concentration Estimates

Estimates of the atom concentrations at the side-arm opening can be made from the titration endpoints under flow tube conditions, however there are two complications: determining the exact endpoint and interpreting the initial rise of the N-atom signal with the addition of small amounts of NO (Fig. 3a.)

The titration endpoints, where the N-atom LIF signal vanishes and the O-atom LIF signal levels off, are roughly 0.04 sccm NO in Fig. 3a and 0.045 sccm NO in Fig. 3c. This difference is likely a reflection of day-to-day repeatability (N-atom and O-atom measurements were conducted on different days), as well as the experimental uncertainty associated with detecting a sharp endpoint.

Below the endpoint in flow tube mode, the O-atom concentration rises linearly from zero with NO addition until the endpoint is reached where all atomic nitrogen has been consumed. Above the endpoint the O-atom concentration

should remain constant. If we choose 0.0425 sccm NO as the average endpoint, the O-atom concentration is computed from the measured temperature, pressure and gas flows as ~2.11×10^{-5} mol m^{-3} with a 1-σ uncertainty of ~25%. It is shown in the following section that O-atom losses on the walls between the titration port and side-arm entrance are small and easily absorbed in this error estimate.

If the $N + NO \rightarrow N_2 + O$ reaction is the dominant reactive process, the O-atom endpoint concentration should also equal the N-atom concentration without added NO. However, the N-atom concentration profiles in Figs. 3a and 3b show an initial sharp *increase* with the addition of small amounts of NO, in contrast to the immediate N-atom loss anticipated from the fast N + NO reaction. Similar behaviors have been documented by other researchers working with fast flow and/or high power nitrogen discharge systems.[23-25]

Two main explanations have been proposed: 1) NO addition causes a reduction in N-atom surface losses, or 2) NO addition catalyzes additional dissociation of electronically or vibrationally-excited nitrogen molecules, N_2*. It is possible to construct kinetic models for both mechanisms that can mimic the experimental observations.[23]

In our system, NO is injected into the flow near the tube centerline and causes a very rapid rise in the N-atom LIF signal even when the concentration of NO is ~10 times lower than the N-atom concentration. In order to decrease heterogeneous losses of N atoms either NO or the O atoms produced by the N + NO reaction must reach the surface and dominate the competition for surface sites. It seems unlikely that NO could dominate surface coverage under these conditions, since N atoms are both in excess and should have a much stronger driving force (energy reduction) for chemisorption. Density functional theory computations by Arasa *et al.*[26], suggest O atoms have a slightly greater adsorption energy on SiO_2 than N atoms, but that both energies are high and initial sticking coefficients are similar.[26] More recent atomistic simulations of Cozmuta[27] predict that O-atom adsorption energies are higher than N-atom adsorption energies on silica surfaces and that O-atom adsorption dominates over N-atom adsorption in gas mixtures containing both species.

The present experiments were carried out at similar total pressures, temperatures and flow rates to those of Copeland *et al.*[9] who did not observe an initial rise in N-atom concentration with added NO. It is possible that they did not collect titration data with sufficient resolution in added NO flow to observe the initial N-atom signal rise. However, our microwave discharge source also operates at much higher powers (2.4 kW vs. 100 W) and is expected to generate much higher concentrations of excited nitrogen species. Any reduction of N-atom surface recombination because of NO addition should be similar in both sets of experiments, however catalytic dissociation of N_2* upon NO addition would be more easily observed in our discharge system.

Within the catalytic dissociation model, the initial rise in the N-atom concentration is explained by a net reaction $NO + N_2^* \rightarrow NO + N + N$, where the reaction rate is faster than the N + NO rate. The subsequent N-atom concentration maximum and a linear decay with added NO is explained by the depletion of N_2*, the concentration of which is presumably lower at the titration port than that of the N atoms. Since the slope of the linear decay then simply reflects removal of N atoms by NO, the endpoint corresponding to the initial N-atom concentration can be estimated from a parallel line (the dashed line in Fig. 3a) as approximately 0.035 sccm, or about 12.5% lower than the observed endpoint. The initial N-atom concentration corresponding to an average observed endpoint of 0.0425 sccm NO is then ~1.84×10^{-5} mol m^{-3}.

C. LIF Signal Corrections

The LIF signal magnitudes collected from each PMT depend on many factors in addition to the local atom concentration, such as optical alignment, PMT sensitivity, filter transmission, and excitation volume and laser beam geometry. For a stable species, these factors can be determined for each PMT by filling the reactor with a uniform static concentration and comparing collected LIF signals, but this is not possible for reactive species like O and N atoms that are lost on the reactor walls. The closest approximation to uniform atom concentrations that can be obtained in our system is under flow tube conditions. However, the signal ratios collected in flow-tube mode still need to be adjusted for differences in atomic concentration at the different PMT locations caused by pressure gradients and heterogeneous atom losses, before they can be used to normalize diffusion tube measurements.

The Hagen-Poiseulli relation[28] can be used together with the ideal gas law, the measured pressures at ports A and B, the measured N_2 flow rates and the known reactor distances to compute the total gas pressure at each PMT location, assuming that molecular nitrogen dominates the transport properties with a viscosity of 17.77×10^{-6} Pa s at 298 K.[29] The bulk flow speed, v, can be computed at each location from the pressure and N_2 flow rate, using mass conservation and the ideal gas law. The atom loss due to heterogeneous recombination between PMT locations are estimated from a simple one-dimensional first-order model that equates the difference in the atom flow between axial location z and $z + dz$ to the losses incurred on the wall over the incremental distance dz:

Table 1 Calculated pressure and concentration ratios in flow tube configuration

PMT	Pressure Ratios	N-atom Concentration Ratios			O-atom Concentration Ratios		
		$\gamma_N = 1\times10^{-5}$	5×10^{-5}	1×10^{-4}	$\gamma_O = 1\times10^{-5}$	5×10^{-5}	1×10^{-4}
1	1	1	1	1	1	1	1
2	0.982	0.979	0.900	0.809	0.980	0.906	0.821
3	0.964	0.959	0.811	0.658	0.962	0.822	0.676
4	0.946	0.940	0.733	0.537	0.943	0.747	0.559

Table 2 Measured and corrected PMT signal ratios in flow tube configuration

PMT	N-atom PMT Signal Ratios		O-atom PMT Signal Ratios	
	Measured	Corrected	Measured	Corrected
1	1	1	1	1
2	1.06	1.10	1.21	1.26
3	2.90	3.14	3.53	3.81
4	0.694	0.780	0.565	0.633

$$\frac{d(vc)}{dz} = -\frac{\gamma\bar{v}}{2R}\bar{c} \ , \tag{1a}$$

where R is the tube radius, c is the atom concentration, v is the bulk flow speed, $\bar{v}$ is the average thermal speed of the atoms $\sqrt{8\Re T/\pi M}$, and γ is the estimated loss probability (the fraction of atom-surface collisions which result in permanent removal of an atom from the gas phase). The value of γ is uncertain, but as a first approximation can be taken in the range ~$1\text{-}10\times10^{-5}$ for O and N atoms on quartz.[12]

Defining the representative atom concentration over dz as $\bar{c} \cong vc/v_{ave}$ allows integration of Eq. (1a) to give

$$\frac{c(z_1)}{c(z_2)} = \frac{v_2}{v_1}\exp\left(-\frac{\gamma\bar{v}(z_2-z_1)}{2Rv_{ave}}\right) = \frac{P_1}{P_2}\exp\left(-\frac{\gamma\bar{v}(z_2-z_1)}{2Rv_{ave}}\right) \ , \tag{1b}$$

where v_{ave} is the average flow velocity between locations z_1 and z_2, and the substitution $v_2/v_1 = P_1/P_2$ follows from the ideal gas law and mass conservation. Equation (1b) allows estimation of the combined effects of pressure difference and wall loss on the local atom concentrations between two PMT positions along the flow tube.

For N-atom LIF calibration, flow tube measurements were made without added NO flow. For O-atom LIF calibration, NO was added just below the titration endpoint. Table 1 lists the pressure ratios for the different PMT locations under our flow conditions, as well as the estimated ratios of atom concentration for different assumed values of γ. Pressure variations are small, amounting to only a few percent. However, wall losses can potentially change the atom concentrations by several 10's of percent along the flow tube, depending on the loss probabilities assumed. We choose the value $\gamma_O = \gamma_N = 1\times10^{-5}$ in our estimates of wall loss and show later that this produces reasonable agreement between simulations and experiment. Table 2 compares the measured PMT signal ratios in flow tube mode to the pressure and wall-loss corrected PMT signal ratios.

Relative atom concentrations during diffusion tube experiments can now be assigned by dividing the LIF data by the corrected PMT signal ratios of Table 2. Figures 4a and 4b show these relative atom concentrations as a function of added NO flow, for N atoms and O atoms, respectively, where the data have been adjusted to the same endpoint of 0.0425 sccm added NO flow. The corresponding N- and O-atom concentrations at the side-arm reactor entrance can be reasonably well approximated by the expressions $c_N = 2.11\times10^{-5}(0.0425 - F_{NO})/0.0415$ and $c_O = 2.11\times10^{-5}\,F_{NO}/0.0425$, where the concentrations are in mol m^{-3} and the NO flows are in sccm.

The goal of the numerical reaction-diffusion model described in the next section is to reproduce the curvatures and relative magnitudes of the experimental N- and O-atom concentrations plotted in Fig. 4, and the corresponding

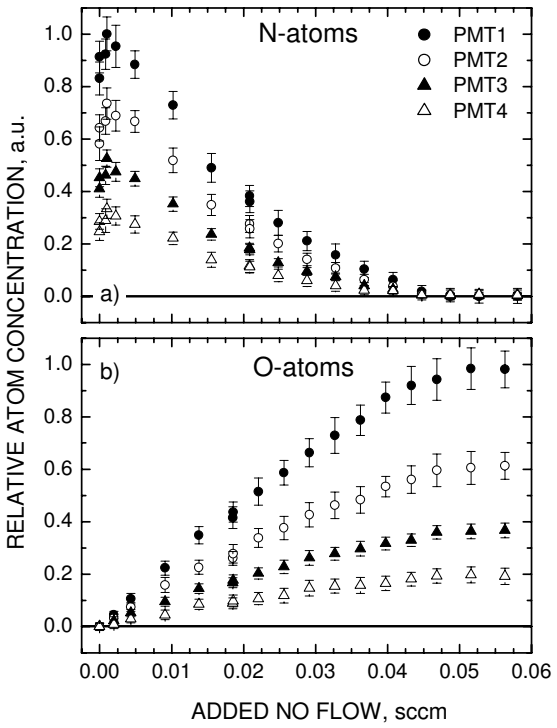

Figure 4. Relative atom concentrations at the different PMT locations during diffusion tube experiments: a) N atoms, and b) O atoms. The error bars are the standard deviations of the collected PMT signals.

scaled data in Fig. 3, using the entrance atom concentrations deduced above and various surface reaction boundary conditions.

IV. Model Formulation

A. Governing Equation, Transport Model, and Chemistry

The side-arm reactor geometry was modeled as tube of length L = 146.7 cm and uniform radius R = 1.1 cm, closed at one end by a disk normal to the tube axis. The governing equation describing two-dimensional cylindrical diffusion-reaction of species s in the side-arm tube is

$$\frac{\partial \rho_s}{\partial t} + \frac{1}{r}\frac{\partial}{\partial r}(r j_{sr}) + \frac{\partial}{\partial z}(j_{sz}) = w_s \,. \tag{2}$$

where ρ_s is the species mass density, w_s represents the rate of species production due to gas-phase chemical reactions, and j_{sr} and j_{sz} are the diffusive mass fluxes in the radial and axial directions relative to the mass average velocity of the mixture. The diffusive mass fluxes in the radial and axial directions are related to the corresponding diffusion velocities by $j_{sr} = \rho_s v_{sr}$ and $j_{sz} = \rho_s v_{sz}$.

Concentration profiles were obtained by the simultaneous solution of the set of 8 species continuity equations (2) for N, O, N_2, O_2, NO, N_2O, NO_2, and O_3. Solution of the momentum and energy equations is not required to obtain concentration profiles under the isothermal and isobaric conditions of the dead-end side-arm reactor. The ideal gas law was used as the equation of state. The species mass flux vector is given by

$$\mathbf{j_s} = -(cM_s D_s)\nabla x_s + \frac{\rho_s}{\rho}\sum_r (cM_r D_r)\nabla x_r \quad , \tag{3}$$

with M_s the species molar mass, x_s the species mole fraction, and D_s the effective binary diffusion coefficient for species s in the gas mixture; c and ρ are the total molar and mass densities of the gas, respectively.

Effective diffusion coefficients in the multi-component gas mixtures of the experiment are computed using the friction-weighted self-consistent effective binary diffusion (SCEBD) approximation[30,31]:

$$D_s = \left(1 - \frac{\omega_s}{\omega}\right)\left(\sum_{r \neq s} \frac{x_r}{D_{r,s}}\right)^{-1} \quad . \tag{4}$$

Different choices are possible for the weighting factor ω_s [30,31]; we choose $\omega_s = x_s$ so that Eq. 4 reduces to the exact binary value for a two-component mixture. The binary diffusion coefficients $D_{r,s}$ for all species pairs are computed from

$$D_{r,s} = \frac{3}{16P\pi\overline{\Omega}_{rs}^{(1,1)}}\sqrt{\frac{2\pi(k_B T)^3 N_{Avro}}{M_{r,s}}} \quad , \tag{5}$$

where $M_{r,s} = M_r M_s/(M_r + M_s)$ and $\pi\overline{\Omega}_{rs}^{(1,1)}$ are collision integrals compiled by Wright *et al.* [32,33]. The collision integrals were implemented using the curve fit formulas of Gupta et al.[34], in a manner identical to that employed in the widely used NASA CFD code, DPLR.[35] Collision integrals for ozone were unavailable, and were approximated by those given for carbon dioxide.

Table 3 Gas-phase reactions

	Reaction	Rate[a]	Refs.
R1	$O + O + M \rightarrow O_2 + M$	$k_1 = (3.1 \pm 1.6)\times 10^{-33}$	36
R2	$O + O_2 + M \rightarrow O_3 + M$	$k_2 = (6.0 \pm 0.6)\times 10^{-34}$	18
R3	$O + O_3 \rightarrow O_2 + O_2$	$k_3 = (8.0 \pm 1.2)\times 10^{-15}$	18
R4	$O + N + M \rightarrow NO + M$	$k_4 = (1.0 \pm 0.5)\times 10^{-32}$	19
R5	$O + NO + M \rightarrow NO_2 + M$	$k_5 = (9.0 \pm 1.8)\times 10^{-32}$	18
R6	$O + NO_2 \rightarrow NO + O_2$	$k_6 = (1.04 \pm 0.15)\times 10^{-11}$	18
R7	$N + N + M \rightarrow N_2 + M$	$k_7 = (4.4 \pm 2.2)\times 10^{-33}$	19
R8	$N + NO \rightarrow N_2 + O$	$k_8 = (3.0 \pm 0.9)\times 10^{-11}$	18
R9	$N + NO_2 \rightarrow N_2O + O$	$k_9 = (1.2 \pm 0.6)\times 10^{-11}$	18

[a] Bimolecular rate constants are in units of cm^3 $molecule^{-1}$ s^{-1}. Termolecular rate constants are in units of cm^6 $molecule^{-2}$ s^{-1}, and the collision partner M is taken as N_2.

Table 3 lists the room-temperature rate coefficients for nine gas phase reactions included in our model involving dissociated oxygen and nitrogen species. The reverse reaction rates are negligibly slow under our experimental conditions and were set to zero.

B. Boundary Conditions and Solution Procedure

The production of species by surface-catalyzed reactions must be balanced by their diffusive flux at the wall:

$$-j_{s,w} = w_{s,w} \tag{6}$$

For *reactant* species the production rates at the surface can be expressed as a loss probability, γ_s, times the surface impingement fluxes; for O and N atoms this gives the production rates (negative for loss)

$$w_{O,w} = -\gamma_O \frac{\rho_{O,w}\bar{v}_O}{4} \quad . \tag{7a}$$

$$w_{N,w} = -\gamma_N \frac{\rho_{N,w}\bar{v}_N}{4} \quad . \tag{7b}$$

The loss probability is defined as *the fraction of impinging reactant flux removed permanently from the gas phase*. It is not a fundamental chemical quantity, rather, it reflects the total efficiency of all operating surface reaction pathways that remove species *s* on a particular surface under a particular combination of temperature, pressure, and gas composition. If the reactant species is consumed to produce more than one product species, branching fractions, $f_{s,r}$, can be defined as the *fraction of impinging reactant removed permanently from the gas phase that participates in forming product species r.* We avoid the common term "recombination coefficient" for γ_s because this term implies a reaction product that is the parent molecule of the reactant (i.e., O_2 for O-atoms), which is clearly not always the case in multi-reactant mixtures.

The absolute lower and upper bounds on both γ_s and $f_{s,r}$ are 0 and 1, but this range may be reduced by other factors such as the availability of partner reactants. For a partially dissociated mixture of oxygen and nitrogen interacting with a catalytic surface via three net steady-state heterogeneous reaction pathways: $O + O \rightarrow O_2$, $N + N \rightarrow N_2$, and $O + N \rightarrow NO$, element conservation dictates the constraint:

$$(1 - f_{O,O_2})\gamma_O \rho_{O,w}\bar{v}_O/M_O = (1 - f_{N,N_2})\gamma_N \rho_{N,w}\bar{v}_N/M_N \; . \tag{8}$$

In the simulations that follow, we demonstrate the effect of NO surface production on the predicted O- and N-atom concentration profiles along the diffusion side-arm tube for different fixed N_2/N/O compositions at the side-arm opening. To achieve this we choose values of γ_O and γ_N, and then vary nitric oxide surface production. When $\gamma_O \rho_{O,w} \bar{v}_O / M_O < \gamma_N \rho_{N,w} \bar{v}_N / M_N$, the level of NO production can be set by choosing $0 \le f_{O,O_2} \le 1$ together with

$$f_{N,N_2} = 1 - (1 - f_{O,O_2})(\gamma_O \rho_{O,w} \bar{v}_O M_N / \gamma_N \rho_{N,w} \bar{v}_N M_O) \quad , \tag{9a}$$

and when $\gamma_O \rho_{O,w} \bar{v}_O / M_O > \gamma_N \rho_{N,w} \bar{v}_N / M_N$, NO production is determined by choosing $0 \le f_{N,N_2} \le 1$ and

$$f_{O,O_2} = 1 - (1 - f_{N,N_2})(\gamma_N \rho_{N,w} \bar{v}_N M_O / \gamma_O \rho_{O,w} \bar{v}_O M_N) \quad . \tag{9b}$$

Nitric oxide surface production is respectively eliminated or maximized when $f_{O,O_2} = 1$ or 0 in Eq. (9a), or when $f_{N,N_2} = 1$ or 0 in Eq. (9b). The individual production rates of the surface reaction products are

$$w_{O_2,w} = -f_{O,O_2} \frac{M_{O_2}}{2M_O} w_{O,w} \tag{10a}$$

$$w_{N_2,w} = -f_{N,N_2} \frac{M_{N_2}}{2M_N} w_{N,w} \tag{10b}$$

$$w_{NO,w} = (f_{N,N_2} - 1)\frac{M_{NO}}{M_N} w_{N,w} = (f_{O,O_2} - 1)\frac{M_{NO}}{M_O} w_{O,w} \quad . \tag{10c}$$

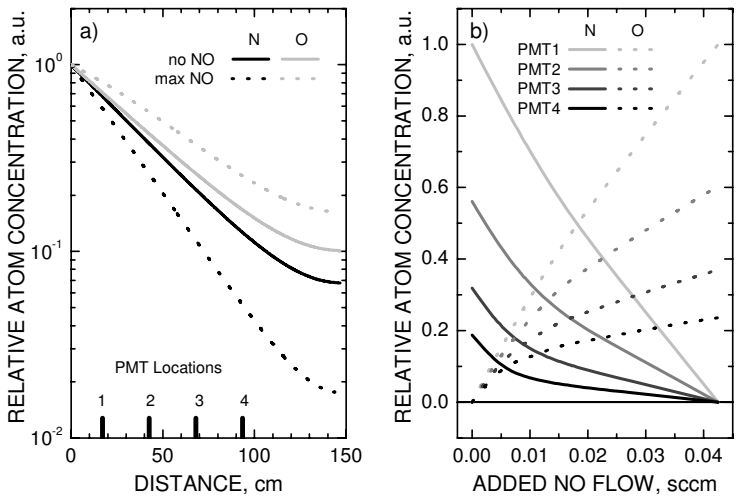

Figure 5. Model simulations for $\gamma_O = \gamma_N = 1 \times 10^{-5}$: a) relative atom concentration profiles along the diffusion tube side-arm at an added NO flow rate of 0.0215 sccm, with or without surface NO production; b) relative atom concentrations at different PMT locations as a function of the flow of added NO, with maximum NO surface production.

Equation (6), together with expressions (7a,b) and (10a-c), provides the species boundary conditions on all the side-arm surfaces at $r = R$ for $z = 0$ to L and at $z = L$ for $r = 0$ to R. A zero-flux boundary condition, $j_{sr} = 0$, was applied along the tube centerline ($r = 0$ for $z = 0$ to L). The gas composition at the side-arm entrance was specified according to the experimental conditions and taken as uniform for $z = 0$ and $r = 0$ to R.

Equation (2) was discretized using a fourth-order accurate finite difference scheme for the spatial derivatives and iterated to steady-state using a third-order accurate Runge-Kutta method. Grid convergence was obtained for grids with 60×10 grid points in the axial and radial directions, respectively. Steady-state solutions were achieved using a CFL number of 1. The CFL number is defined as the ratio of the

simulation time step, Δt, to the minimum physical diffusion time scale in the flow, Δt_{diff}, where $\Delta t_{diff} = \rho\left(\Delta z^2 + \Delta r^2\right)/\mu$ and Δz and Δr are the grid spacings in the axial and radial directions, respectively. The simulations that follow were all computed using a 60 × 10 grid and a CFL number of 1.

V. Simulation Results

Simulations were computed for T = 298 K, P = 60 Pa, and various O-atom and N-atom concentrations at the side-arm entrance corresponding to NO titration flows in the range 0.0 to 0.0425 sccm, with the balance assumed to be molecular nitrogen. The concentrations of all other species were set to zero at the entrance.

Figure 5a shows relative atom concentration profiles along the dead end diffusion tube computed for an NO titration flow of 0.0215 sccm and the loss probabilities $\gamma_O = \gamma_N = 1\times10^{-5}$. The solid lines show the decay of N- and O-atom concentrations along the diffusion tube when no surface NO production is allowed. Though the loss probabilities are set equal for N and O atoms in this simulation, N atoms are lost more rapidly down the side-arm tube than O atoms because the lighter N atoms collide with the surface more often and have a lower diffusion coefficient in molecular nitrogen (about 522 vs. 628 cm^2 s^{-1}). The corresponding profiles when NO surface production is maximized (dotted lines), show that the loss rate of N atoms increases and the loss rate of O atoms decreases.

With surface NO production eliminated, the same concentration profiles (Fig. 5a, solid lines) are produced whether or not gas-phase chemistry is included in the computations. With surface NO production maximized and the N + NO gas phase reaction eliminated, computed O- and N-atom profiles again overlay the profiles for no NO surface production (solid lines). Taken together, these modelling results support the mechanism proposed by Copeland *et al.*[9], that requires both surface production of NO and the N + NO gas-phase reaction to explain the experimental measurements.

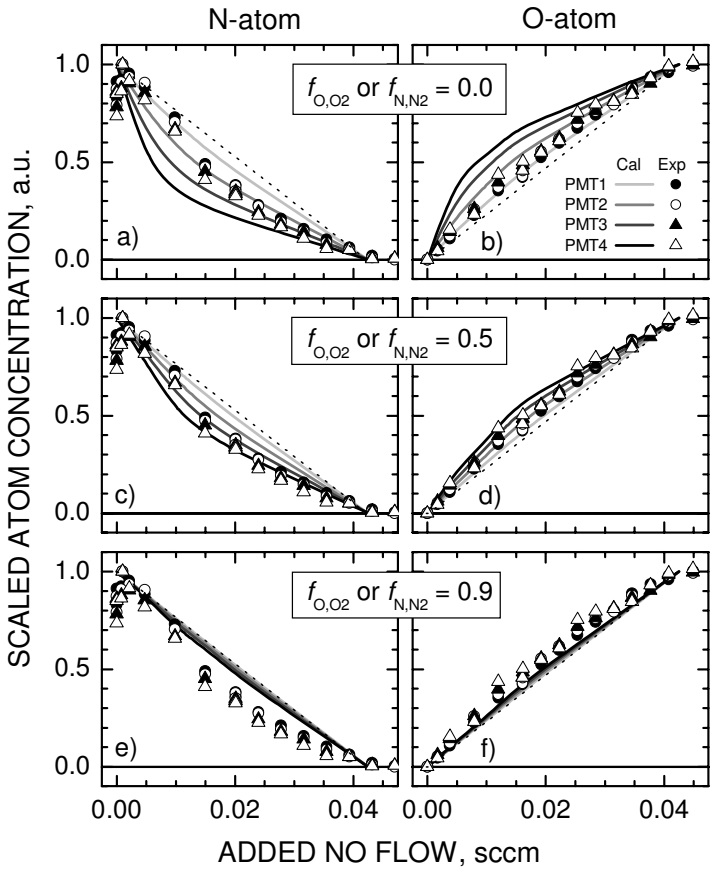

Figure 6. Experimental (symbols) and computed (lines) scaled atom concentrations at the four PMT locations as functions of added NO flow. Computations with $\gamma_O = \gamma_N = 1 \times 10^{-5}$ and a), b) maximum, c), d) intermediate, and e), f) minor NO surface production. Dotted lines show a linear dependence for reference.

In Fig. 5b, we show the relative N-atom (solid lines) and O-atom (dotted lines) concentrations computed at the different PMT locations as a function of added NO flow. These computations were made assuming maximum NO surface production and $\gamma_O = \gamma_N = 1\times10^{-5}$. Comparison with the experimental data of Fig. 4 shows generally good agreement, keeping in mind that the initial rise of N-atoms with NO addition is not included in the reaction-diffusion model. Relative atom concentrations under un-titrated and fully-titrated conditions are independent of surface or gas-phase NO chemistry. Model predictions using $\gamma_O = \gamma_N = 1\times10^{-5}$ reproduce measured relative atom concentrations at 0 and 0.0425 sccm added NO fairly well. Much poorer agreement is obtained for higher loss probabilities like $\gamma_O = \gamma_N = 5\times10^{-5}$ which predict atom

losses much greater than those observed experimentally.

Figures 6a-f compare experimental scaled N-atom and O-atom concentrations to numerical predictions assuming $\gamma_O = \gamma_N = 1\times10^{-5}$ and different levels of NO surface production. The experimental data have been scaled to align (approximately) the experimental and computational endpoints at 0 sccm (no O atoms) and 0.0425 sccm (no N atoms). Figures 6a and 6b show that the model computations with maximum NO surface production reproduce the concave and convex curvatures observed in the experimental diffusion tube data for both N and O atoms. However, the predicted differences in curvature between four PMT locations are much larger than observed, suggesting that the maximum surface NO production condition is too extreme.

A similar comparison is shown in Figs. 6c and 6d, for calculations that enforce a more moderate NO surface production condition, by setting either $f_{O,O_2} = 0.5$ in Eq. 9a or $f_{N,N_2} = 0.5$ in Eq. 9b. The computed profiles now show a tighter spread in curvature, more in line with experimental observation, especially for oxygen atoms. While the quality of agreement depends somewhat on the scaling used to align the experimental and computed endpoints, the general observations of the experiment are well reproduced.

Figures 6e and 6f show computational results when NO surface production is a minor pathway (either $f_{O,O_2} = 0.9$ in Eq. 9a or $f_{N,N_2} = 0.9$ in Eq. 9b.) The profiles show much less curvature, approaching the linear dependence indicted by the dotted line, and compress the differences in curvature between the four PMT locations further. These simulations do not reproduce the experiment as well as those of Figs 6c and 6d, indicating that NO surface production is not a minor pathway in our experiment, but rather comparable in magnitude to the O + O and N + N surface recombination pathways.

The reaction-diffusion model used to simulate the diffusion tube experiments is only constrained by element conservation and does not include finite-rate surface chemistry. This type of model is often used for parametric studies seeking to bound catalytic effects[37], but lacks physics-based kinetic formulations that describe intermediate catalytic behavior under transient thermal and flow environments. A more attractive approach for including the NO surface formation in CFD computations is with a finite-rate surface chemistry model as implemented by Kurotaki[5] and others[1-4,6,7]; i.e., a model that incorporates kinetic mechanisms like adsorption, thermal desorption, Eley-Rideal recombination and Langmuir-Hinschelwood recombination. Unfortunately, these models contain large numbers of numerical parameters that must be chosen by theory and/or adjusted to reproduce experiment data. More experimental data are required, at higher temperatures and over a larger range of gas pressures and compositions, to enable the construction of a suitable finite-rate chemistry model for our experiments. Such measurements are currently underway in our laboratory.

VI. Summary

The experimental results presented here support the surface-catalyzed production of nitric oxide from the recombination of atomic oxygen and atomic nitrogen on quartz. Computational simulations of the side-arm reactor with a multi-species reaction-diffusion model, incorporating NO surface production and gas phase reaction of NO and N atoms, qualitatively reproduce the experimental observations, and suggest that NO surface formation is of comparable magnitude to the O + O and N + N surface recombination reactions.

Together with the CFD simulations of Kurotaki[5] that indicate the importance of NO surface formation in matching computational and measured heating data for the OREX flight, and the LIF detection of NO over different material surfaces during plasma testing by Laux et al.[8], the present work strengthens the case for including O + N surface recombination in CFD simulations of hypersonic flight and plasma testing.

Acknowledgments

This work was supported jointly by the Ceramics and Nonmetallic Materials Program and the Hypersonics Program of the Air Force Office of Scientific Research through the prime contract FA9556-05-1-10490. We thank Richard Copeland for helpful discussions and Michael Wright for providing the collision integrals used in our computations. Jochen Marschall acknowledges the late Joan Pallix for inspiring this line of research..

References

[1]Natsui, F., Barbato, M., and Bruno, C., "Material-Dependent Catalytic Recombination Modeling for Hypersonic Flows," *Journal of Thermophysics and Heat Transfer*, Vol. 10, 1996, pp. 131-136.

[2]Daiß, A., Frühauf, H.-H., and Messerschmid, E.W., "Modeling Catalytic Reactions on Silica Surfaces with Consideration of Slip Effects," *Journal of Thermophysics and Heat Transfer*, Vol. 11, 1997, pp. 346-352.

[3]Deutschmann, O., Riedel, U., and Warnatz, J., "Modeling of Nitrogen and Oxygen Recombination on Partial Catalytic Surfaces," *Journal of Heat Transfer*, Vol. 117, 1995, pp. 495-501.

[4]Kovalev, V.L., Suslov, O.N., and Triskiy, G.A., "Phenomenological Theory for Heterogeneous Recombinationof Partially Dissociated Air on High-Temperature Surfaces," in *Molecular Physics and Hypersonic Flows*, edited by M. Capitelli, (Kluwer Academic, Boston, 1996), p. 193-202.

[5]Kurotaki, T., "Catalytic Model on SiO_2-Based Surface and Application to Real Trajectory," *Journal of Spacecraft and Rockets*, Vol. 38, 2001, pp. 798-800.

[6]Armenise, I., Barbato, M., Capitelli, M., and Kustova, E., "State-to-State Catalytic Models, Kinetics, and Transport in Hypersonic Boundary Layers," *Journal of Thermophysics and Heat Transfer*, Vol. 20, 2006, pp. 465-476.

[7]Daiß, A., Frühauf, H.-H., and Messerschmid, E.W., "Chemical Reactions and Thermal Nonequilibrium on Silica Surfaces," in *Molecular Physics and Hypersonic Flows*, edited by M. Capitelli, (Kluwer Academic, Boston, 1996), p. 203-218.

[8]Laux, T., Feigl, M., Stöckle, T., and Auweter-Kurtz, M., "Estimation of the Surface Catalyticity of PVD-Coatings by Simultaneous Heat Flux and LIF Measurements in High Enthalpy Air Flows," AIAA Paper 2000-2364, June 2000.

[9]Copeland, R.A., Pallix, J.B., and Stewart, D.A., "Surface Catalyzed Production of NO from Recombination of N and O Atoms," *Journal of Thermophysics and Heat Transfer*, Vol. 12, 1998, pp. 496-499.

[10]Smith, W.V., "The Surface Recombination of H Atoms and OH Radicals," *Journal of Chemical Physics*, Vol. 11, 1943, pp. 110-125.

[11]Wise, H. and Wood, B.J., "Reactive Collisions Between Gas and Surface Atoms," in *Advances in Atomic and Molecular Physics*; *Vol. 3*, edited by D. R. Bates and I. Estermann, (Academic Press, New York, 1967), p. 291-353.

[12]Pallix, J.B. and Copeland, R.A., "Measurement of Catalytic Recombination Coefficients on Quartz Using Laser-Induced Fluorescence," *Journal of Thermophysics and Heat Transfer*, Vol. 10, 1996, pp. 224-233.

[13]Kim, Y.C. and Boudart, M., "Recombination of O, N, and H Atoms on Silica: Kinetics and Mechanism," *Langmuir*, Vol. 7, 1991, pp. 2999-3005.

[14]Marschall, J., "Experimental Determination of Oxygen and Nitrogen Recombination Coefficients at Elevated Temperature Using Laser-Induced Fluorescence," AIAA Paper 97-3879, August 1997.

[15]Marschall, J., Chamberlain, A., Crunkleton, D., and Rogers, B., "Catalytic Atom Recombination on ZrB_2/SiC and HfB_2/SiC Ultra-High Temperature Ceramic Composites," *Journal of Spacecraft and Rockets*, Vol. 41, 2004, pp. 576-581.

[16]Marschall, J., Copeland, R.A., Hwang, H.H., and Wright, M.J., "Surface Catalysis Experiments on Metal Surfaces in Oxygen and Carbon Monoxide Mixtures," AIAA Paper 2006-181, January 2006.

[17]Sepka, S., Chen, Y.-K., Marschall, J., and Copeland, R.A., "Experimental Investigation of Surface Reactions in Carbon Monoxide and Oxygen Mixtures," *Journal of Thermophysics and Heat Transfer*, Vol. 14, 2000, pp. 45-52.

[18]Sander, S.P., Friedl, R.R., Golden, D.M., Kurylo, M.J., Moortgat, G.K., Wine, P.H., Ravishankara, A.R., Kolb, C.E., Molina, M.J., Finlayson-Pitts, B.J., Huie, R.E., and Orkin, V.L., "Chemical Kinetics and Photochemical Data for Use in Atmospheric Studies: Evaluation Number 15," JPL Publication 06-2, July 10, 2006.

[19]Baulch, D.L., Drysdale, D.D., and Horne, D.G., *Evaluated Kinetic Data for High Temperature Reactions, Volume 2: Homogeneous Gas Phase Reactions of the H_2-N_2-O_2 System*, Butterworths, London, 1973.

[20]Bischel, W.K., Perry, B.E., and Crosley, D.R., "Detection of Fluorescence from O and N Atoms Induced by Two-Photon Absorption," *Applied Optics*, Vol. 21, 1982, pp. 1419-1428.

[21]Bischel, W.K., Perry, B.E., and Crosley, D.R., "Two-Photon Laser-Induced Fluorescence in Oxygen and Nitrogen Atoms," *Chemical Physics Letters*, Vol. 82, 1981, pp. 85-88.

[22]Adams, S.F. and Miller, T.A., "Two-Photon Absorption Laser Induced Fluorescence of Atomic Nitrogen by an Alternative Excitation Scheme," *Chemical Physics Letters*, Vol. 295, 1998, pp. 305-311.

[23]Repsilber, T. and Uhlenbusch, J., "Absolute Calibration of TALIF of Atomic Nitrogen by NO Titration - Experimental and Theoretical Analysis," *Plasma Chemistry and Plasma Processing*, Vol. 24, 2004, pp. 373-392.

[24]Von Weyssenhoff, H. and Patapoff, M., "Validity and Limitations of the Gas Titration of Atomic Nitrogen with Nitric Oxide," *Journal of Physical Chemistry*, Vol. 69, 1965, pp. 1756-1758.

[25]Young, R.A., Sharpless, R.L., and Stringham, R., "Catalyzed Dissociation of N_2 in Microwave Discharges. I," *Journal of Chemical Physics*, Vol. 40, 1964, pp. 117-119.

[26]Arasa, C., Gamallo, P., and Sayós, R., "Adsorption of Atomic Oxygen and Nitrogen at β-Crisobalite (100): A Density Functional Theory Study," *Journal of Physical Chemistry B*, Vol. 109, 2005, pp. 14954-14964.

[27]Cozmuta, I., "Molecular Mechanisms of Gas Surface Interactions in Hypersonic Flow," AIAA Paper 2007-4046, June 2007.

[28]Schlichting, H., *Boundary-Layer Theory*, McGraw-Hill, New York, 1979.

[29]Touloukian, Y.S., Saxena, S.C., and Hestermans, P., *Thermophysical Properties of Matter. Viscosity*, Vol. 11 IFI/Plenum, New York, 1975.

[30]Ramshaw, J.D., "Self-Consistent Effective Binary Diffusion in Multicomponent Gas Mixtures," *Journal of Non-Equilibrium Thermodynamics*, Vol. 15, 1990, pp. 295-300.

[31]Ramshaw, J.D. and Chang, C.H., "Friction-Weighted Self-Consistent Effective Binary Diffusion Approximation," *Journal of Non-Equilibrium Thermodynamics*, Vol. 21, 1996, pp. 223-232.

[32]Wright, M.J., Bose, D., Palmer, G.E., and Levine, E., "Recommended Collision Integrals for Transport Property Computations I: Air Species," *AIAA Journal*, Vol. 43, 2005, pp. 2558-2564.

[33]Wright, M.J., Hwang, H.H., and Schwenke, D.W., "Recommended Collision Integrals for Transport Property Computations Part 2: Mars and Venus Entries," *AIAA Journal*, Vol. 45, 2007, pp. 281-288.

[34]Gupta, R., Yos, J., Thompson, R., and Lee, K., "A Review of Reaction Rates and Thermodynamic and Transport Properties for an 11-Species Air Model for Chemical and Thermal Nonequilibrium Calculations to 30000 K," NASA RP-1232, August 1990.

[35]Wright, M.J., Candler, G.V., and Bose, D., "Data-Parallel Line Relaxation Method for the Navier-Stokes Equations," *AIAA Journal*, Vol. 36, 1998, pp. 1603-1609.

[36]Baulch, D.L., Drysdale, D.D., Duxbury, J., and Grant, S.J., *Evaluated Kinetic Data for High Temperature Reactions, Volume 3. Homogeneous Gas Phase Reactions of the O_2-O_3 system, the CO-O_2-H_2 system, and of Sulfur-Containing Species.*, Butterworths, London, 1976.

[37]Bose, D. and Wright, M., "Uncertainty Analysis of Laminar Aeroheating Predictions for Mars Entries," AIAA Paper 2005-4682, June 2005.